remote sensing

Article

Aerosol Indices Derived from MODIS Data for Indicating Aerosol-Induced Air Pollution

Junliang He [1,2], Yong Zha [1],*, Jiahua Zhang [3],* and Jay Gao [4]

[1] Key Laboratory of Virtual Geographic Environment, Ministry of Education, College of Geographic Science, Nanjing Normal University, Nanjing 210097, China; E-Mail: hejunliang0927@163.com

[2] Department of Resources and Environment, Shijiazhuang University, Shijiazhuang 050035, China

[3] Lab. of Digital Earth Sciences, Institute of Remote Sensing and Digital Earth, Chinese Academy of Sciences, Beijing 100094, China

[4] School of Environment, University of Auckland, Auckland 1008, New Zealand; E-Mail: jg.gao@auckland.ac.nz

* Author to whom correspondence should be addressed; E-Mails: yzha@njnu.edu.cn (Y.Z.); jhzhang@ceode.ac.cn (J.Z.); Tel.: +86-25-8589-8500 (Y.Z.), +86-10-8217-8122 (J.Z.); Fax: +86-25-8589-1347 (Y.Z.), +86-10-8217-8009 (J.Z.).

Abstract: Aerosol optical depth (AOD) is a critical variable in estimating aerosol concentration in the atmosphere, evaluating severity of atmospheric pollution, and studying their impact on climate. With the assistance of the 6S radiative transfer model, we simulated apparent reflectancein relation to AOD in each Moderate Resolution Imaging Spectroradiometer (MODIS) waveband in this study. The closeness of the relationship was used to identify the most and least sensitive MODIS wavebands. These two bands were then used to construct three aerosol indices (difference, ratio, and normalized difference) for estimating AOD quickly and effectively. The three indices were correlated, respectively, with *in situ* measured AOD at the Aerosol Robotic NETwork (AERONET) Lake Taihu, Beijing, and Xianghe stations. It is found that apparent reflectance of the blue waveband (band 3) is the most sensitive to AOD while the mid-infrared wavelength (band 7) is the least sensitive. The difference aerosol index is the most accurate in indicating aerosol-induced atmospheric pollution with a correlation coefficient of 0.585, 0.860, 0.685, and 0.333 at the Lake Taihu station, 0.721, 0.839, 0.795, and 0.629 at the Beijing station, and 0.778, 0.782, 0.837, and 0.643 at the Xianghe station in spring, summer, autumn and

winter, respectively. It is concluded that the newly proposed difference aerosol index can be used effectively to study the level of aerosol-induced air pollution from MODIS satellite imagery with relative ease.

Keywords: aerosol indices; air pollution; 6S model; MODIS

1. Introduction

Aerosols refer to solid or liquid particulates suspended in the atmosphere. As they strongly absorb and scatter solar radiation over the ultraviolet, visible light, and infrared spectrum, they exert a significant influence on global climate and weather processes [1,2]. A rise in the quantity of aerosols in the atmosphere worsens air quality, which in turn, has a detrimental impact on human health [3–5].

Of all the factors indicative of the physical characteristics of aerosols, aerosol optical depth (AOD, a measure of the columnar extinction of solar radiation by aerosols) is an important optical parameter in estimation of aerosol concentration, evaluation of the level of atmospheric pollution, and assessment of the climate effect of aerosols. AOD can be determined using two methods, ground-based monitoring and via satellite imagery. Ground-based determination involves direct measurement using different instruments, as the Multifilter Rotating Shadowband Radiometer (MFRSR), the Lambda Instruments Corporation (LICOR) spectroradiometer, the Microtops Sun photometer, Linke-Feussner actinometers and light detection and ranging (LIDAR). Nevertheless, Cienciae Investigación Médica Estudiantil Latinoamericana (CIMEL) sunphotometer is the most employed instrument for characterizing the column integrated AOD. This method is able to yield accurate readings of aerosol, but is constrained by data availability at certain fixed positions only. Such point-specific data are unable to yield a detailed pattern of aerosol spatiotemporal distribution. By comparison, the satellite remote sensing method is able to generate results over an extensive area in real-time. The gained results can be updated periodically at a relatively short span. Such advantages make this method a vital addition to supplement ground-based measurement so as to gather accurate aerosol information effectively and quickly.

Over recent years a large number of achievements have been accomplished in retrieving AOD from satellite imagery, with many kinds of retrieval algorithms developed, such as the dark-target method [6], the structure function method [7,8], polarization measurements [9,10], the multi-angle method [11,12], and the deep blue algorithm [13]. Common to all of these methods is the complex retrieval process, but each has its own special applicability. For instance, the dark-object method is more accurate in areas of dense vegetation cover. The structure function method requires information on a clear background, and its retrieval accuracy is higher in areas of a bright ground surface.

In remote sensing characteristic indexing has been a rather simple but highly effective method of extracting information from images as the ground object of interest is likely to exhibit different spectral characteristics over different wavebands. For instance, the distinctive reflectance and absorption of vegetation, water, and built-up areas in different wavelengths has been used to derive normalized difference vegetation index (NDVI) that is able to capture vegetation distribution effectively [14], normalized difference water index (NDWI) that is indicative of water distribution [15], and normalized difference built-up index (NDBI) indicating the distribution of built-up areas and barren ground [16].

The construction of these indices is underpinned by the principle of locating the most sensitive and insensitive spectral bands among all multispectral bands available [17]. Of these two bands, the most sensitive is treated as the numerator, and the most insensitive as the denominator. Ratioing of the two bands artificially enlarges the spectral dissimilarity among all ground features drastically. Consequently, information on the target of interest is maximally enhanced on the newly derived index image while information of other background objects in the same image is suppressed simultaneously.

Apparent reflectance as recorded on satellite imagery depends on both surface and atmospheric composition. Therefore, it is possible to retrieve the physical and chemical properties of aerosols from the variation in apparent reflectance caused by aerosol backscattering. Griggs [18] found that the amount of solar radiation vertically reflected over the ocean surface increases almost linearly with AOD. The National Oceanic and Atmospheric Administration (NOAA) started to monitor AOD over oceans in 1977 using the first visible light channel (0.63 μm) of Advanced Very High Resolution Radiometer (AVHRR). Durkee *et al.* [19] demonstrated that radiation detected in the red and near infrared wavebands of satellite imagery is correlated positively with maritime AOD. Hsu *et al.* [20] reported that the Total Ozone Mapping Spectrometer (TOMS)-derived absorbing aerosol index (difference in reflectance between the violet 340 nm and 380 nm channels) is highly consistent with the spatiotemporal pattern of AOD after analyzing the AOD data collected with a sun photometer on the ground during the burning season of bio-substances in South America. After deriving difference vegetation index (DVI) from NOAA AVHRR data, Yu *et al.* [21] constructed a relationship between DVI and PM_{10} so that the latter can be retrieved from the former via the established relationship quantitatively. Zha *et al.* [22] put forward a normalized difference haze index (NDHI) for studying atmospheric haze weather from winter Moderate Resolution Imaging Spectroradiometer (MODIS) imagery. These methods are common in that *in situ* measured data were statistically analyzed to establish the relationship between apparent reflectance and the physical and chemical properties of aerosols. Such empirical statistical relationship faces limitations as it is subject to the influence of the underlying surface, atmospheric conditions, as well as the observation conditions.

In this study the response of apparent reflectance in each of the MODIS wavebands 1–7 to AOD that has been simulated using the Second Simulation of the Satellite Signal in the Solar Spectrum (6S) radiative transfer model is first assessed. A comparison among the seven responses reveals the most and least sensitive MODIS wavebands. These two bands were then used to construct three aerosol indices that can be easily derived from remotely sensed imagery, for the effective detection of atmospheric aerosol pollution with relative ease. The relationship between *in situ* measured AOD at the Lake Taihu, Beijing, and Xianghe stations in the Aerosol Robotic NETwork (AERONET) over one year with the proposed aerosol indices was analyzed to validate the applicability of the proposed aerosol indices in estimating atmospheric pollution caused by aerosols.

2. Data and Method

2.1. Data Acquisition and Processing

The Lake Taihu observation station in the AERONET is located at Northern Taihu (31°25'15"N, 120°12'5"E) in close proximity to the lake water at a sea level of 20 m. The equipment deployed is a fully automatic sun photometer (CE-318). It records the direct solar radiation within a view field of

1.5 ° every 3 min at wavelengths of 340, 380, 440, 500, 670, 870, 936, 1,020, and 1,640 nm. The radiation data collected at the 936 nm waveband was used to acquire the total water vapor in the atmosphere while the data at all other wavebands were used to retrieve AOD with a retrieval error estimated at around 0.01–0.02 [23,24]. In this study the level 2.0 aerosol data over the period of September 2011–August 2012 were downloaded from the AERONET website [25]. Included in the downloaded data are the Direct Sun product (spectral AOD) and the Almucantar inversion product (single scattering albedo—SSA, and asymmetry factor—ASY) [26].

The MODIS sensor is one of a suite of instruments of both the EOS-Terra and EOS-Aqua satellites. These two satellites have a sun-synchronous, polar orbit. Terra has a morning overpass (local time), while Aqua has an afternoon overpass. Standard data products used in this study were downloaded from the National Aeronautics and Space Administration (NASA) website [27]. Such data products as MODIS L1B (MOD02HKM, MYD02HKM), MODIS Geolocation (MOD03, MYD03) and Nadir Reflectance (MCD43A4) over the period of September 2011–August 2012 were downloaded. MOD02HKM (Terra) and MYD02HKM (Aqua) data contain calibrated Earth View observations from MODIS bands 1–7 (centered near 0.66 μm, 0.86 μm, 0.47 μm, 0.55 μm, 1.24 μm, 1.64 μm, 2.13 μm, respectively) at 500-m resolution. The radiance measured by MODIS at high spatial resolution provides improved and valuable information about the physical structure of the Earth's atmosphere and surface. Geolocation data (termed MOD03 and MYD03 for Terra and Aqua, respectively) contain geodetic coordinates, ground elevation, solar and satellite zenith, and azimuth angles for each MODIS 1-km sample. MCD43A4 provides 500-m reflectance data adjusted using a bidirectional reflectance distribution function (BRDF) to model the values as if taken from the nadir view. The MODIS Conversion Toolkit module was used to project these data products to the Universal Transverse Mercator (UTM) (zone 51) coordinate system (Datum: WGS84), during which the bowtie effect was also corrected. The MODIS Geolocation data were resampled spatially to a resolution of 500 m, the same as that of reflectance data. Since the reflectance data provided in the MODIS L1B data product are not normalized by the cosine of the solar zenith angle, it is imperative to modify solar zenith during image processing [28]. Namely, the reflectance recorded under different solar zeniths must be converted to reflectance when the sun is at the zenith using the following equation:

$$\mathrm{Ref}' = \mathrm{Ref} / \cos\theta \tag{1}$$

where Ref refers to the raw reflectance; Ref' stands for the modified reflectance; and θ is the solar zenith angle.

In order to standardise the comparison of ground-based observations with instant satellite-observed data at a given moment, the apparent reflectance and surface reflectance within an area of 2.5 km by 2.5 km centered at the Taihu observation station were averaged. Similarly, the ground-based data recorded within half an hour of the satellite overpass on cloud-free days were also averaged to derive AOD at the 550 nm wavelength using the Angström formula for validating satellite-based results [29]. Over the period of September 2011–August 2012, a total of 148 pairs of data were found useful, of which 40 pairs were in spring (March–May); 36 in summer (June–August), 33 in autumn (September–November), and 39 in winter (December–February).

2.2. Simulation Experiments

The Second Simulation of the Satellite Signal in the Solar Spectrum, commonly known as the 6S radiative transfer model, is able to accurately simulate the atmospheric influence along the path of sun-target-sensor. It is one of the most successful models developed so far for atmospheric correction [30]. This model was applied to simulate the variation of the apparent reflectance of MODIS channels 1–7 with AOD and surface reflectance. In all simulations the geometric parameters of observation were set at 45° for the solar zenith, 30° for the satellite zenith, and 120° for the relative azimuth. The mid-latitude summer atmospheric profile model was adopted for both the spring and summer seasons while the mid-latitude winter atmospheric profile model was used for the autumn and winter seasons. AOD varied between 0.1 and 1.9 at an increment of 0.1; The ground surface was specified as homogeneous Lambertian.

Specification of aerosol type is an important source of errors in retrieving AOD. Thus, it is vital to first determine the aerosol type that is the most appropriate for the study site prior to AOD retrieval [31]. The 6S model provides single scattering albedo (SSA) and asymmetry parameter (ASY) in every waveband for continental and urban type aerosols under standard radiation atmosphere (SRA) for reference [32]. Listed in Table 1 are the retrieved monthly mean SSA and ASY at the Taihu observation station between September 2011 and August 2012. With reference to these values, the data observed at the Taihu station bear a high resemblance to the scattering properties of continental type aerosol in the 6S model. Zhang *et al.* [33] pointed out that in studying the optical properties of aerosols over continental China by means of remote sensing, continental type aerosol in the standard radiation atmosphere depicts the situation more realistically. Therefore, it was decided to adopt the continental type aerosol in this study.

Table 1. Monthly mean single scattering albedo and asymmetry coefficient retrieved from the sun photometer measurements at the Lake Taihu station.

Month	440 nm		675 nm		870 nm		1,020 nm	
	SSA	ASY	SSA	ASY	SSA	ASY	SSA	ASY
2011-SEP	0.918	0.734	0.919	0.666	0.910	0.628	0.906	0.619
2011-OCT	0.892	0.723	0.911	0.651	0.911	0.620	0.910	0.615
2011-NOV	0.908	0.736	0.928	0.666	0.927	0.629	0.925	0.613
2011-DEC	0.869	0.720	0.897	0.642	0.897	0.612	0.892	0.599
2012-JAN	0.924	0.722	0.939	0.649	0.936	0.618	0.928	0.604
2012-FEB	0.911	0.716	0.928	0.650	0.925	0.629	0.918	0.621
2012-MAR	0.907	0.702	0.933	0.642	0.938	0.632	0.938	0.637
2012-APR	0.896	0.706	0.929	0.661	0.938	0.655	0.940	0.661
2012-MAY	0.935	0.715	0.947	0.650	0.946	0.623	0.945	0.619
2012-JUN	0.944	0.721	0.960	0.659	0.961	0.627	0.960	0.613
2012-JUL	0.980	0.707	0.984	0.646	0.983	0.623	0.982	0.629
2012-AUG	0.976	0.759	0.978	0.684	0.975	0.639	0.972	0.618
Mean	0.922	0.722	0.938	0.656	0.937	0.628	0.935	0.621

3. Results

3.1. AOD Variation

The CE-318 sun photometer measured AOD data were averaged, and the seasonal variations of AOD are given in Table 2. An overview of the yearly observations shows that AOD in all four seasons is higher than 0.5, indicating that the atmosphere in the Taihu region is rather murky. Summer AOD is the highest while winter AOD is the lowest. Of the four seasons, both summer and autumn have a relatively large standard deviation in AOD, suggesting that AOD tends to change more in these two seasons. Summer and autumn are the rainy seasons in this region when the weather changes rather abruptly and drastically, triggering a huge change in AOD. In the winter and spring seasons, near surface air is relatively stable, causing little change in AOD during these seasons.
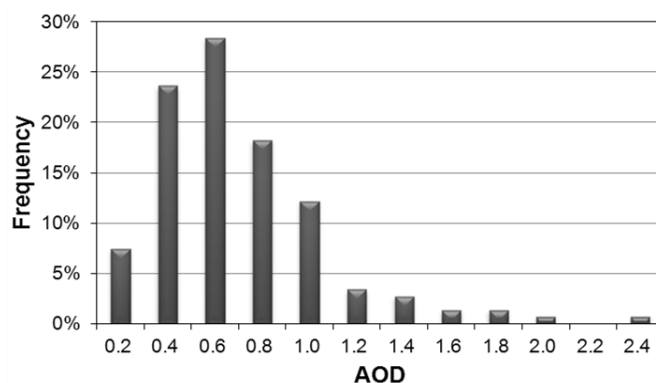
Shown in Figure 1 is the frequency distribution of AOD values over September 2011–August 2012. It illustrates that the highest frequency of year-long AOT occurs within 0.6–0.8, accounting for 28% of the total. Those observations having a relatively high AOD (>0.8) comprise 41% of the total. Those extremely high AOD values (AOD > 1.6) make up only 4% of the total samples. The yearly average AOD stands at 0.59, lower than the mean averaged over multiple years (0.80) [34].

It should be noted that the data statistics above are results from the ground-based data recorded within half an hour of the satellite overpass on cloud-free days. The statistics for all of the level 2.0 AOD retrieved from the direct solar radiation observed at the Lake Taihu station is shown in the Appendix (Table A1). The yearly average AOD stands at 0.55, and it is found that the seasonal change tendency of the AOD is also similar as showed in Table 2.

Table 2. Seasonal variations in aerosol optical depth (AOD) (550 nm) as observed at the Lake Taihu station.

Season	No. of Observations	Seasonal Mean
Spring	40	0.59 ± 0.21
Summer	36	0.68 ± 0.61
Autumn	33	0.63 ± 0.35
Winter	39	0.50 ± 0.17

Figure 1. Frequency distribution of AOD recorded over September 2011–Augst 2012 at the Lake Taihu station.

3.2. Spectral Properties of the Study Site

MODIS nadir observed surface reflectance product (MCD43A4) is derived from 16 consecutive observations that have been calibrated using the surface BRDF model. Since the impact of atmosphere and observation angle has been removed from the data product, it can be treated as the surface reflectance. Illustrated in Figure 2 are the seasonal variations of retrieved surface reflectance from MODIS bands 1–7. In order to facilitate subsequent discussion, the horizontal axis has been arranged by wavelength in the ascending order. The general shape of the spectral response is highly reminiscent of vegetation spectral response with an apparent distinction among the four seasons. In the summer season, there is an obvious disparity in bands 1 (0.66 μm) and 2 (0.86 μm) used in vegetation index (NDVI). The surface reflectance curve in spring and autumn has a similar distribution. In winter the difference between different wavebands becomes noticeably less distinctive than in other seasons. In particular, those wavebands that are used in deriving vegetative index show a markedly subdued effect.

Shown in Figure 3 is the variation of apparent reflectance with wavelength in four seasons. Its comparison with Figure 2 reveals that apparent reflectance is markedly higher in every waveband, especially in those visible light wavebands. The increase is attributed to the stronger atmospheric effect in short wavelengths that has caused a rise of varying magnitude in apparent reflectance.

Figure 2. Variation of surface reflectance as recorded in the seven MODIS wavebands in four seasons.
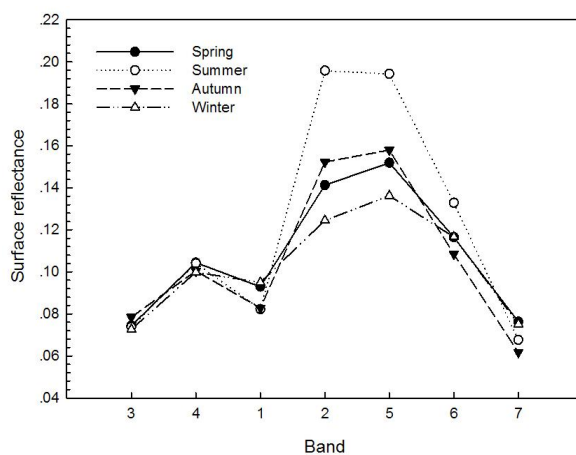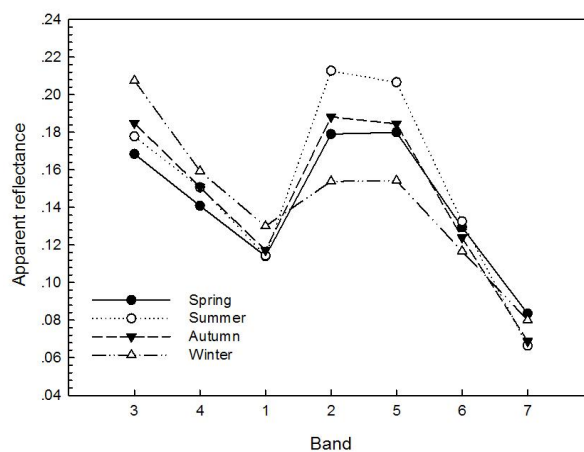

Figure 3. Variation of apparent reflectance with seven MODIS wavebands in four seasons.
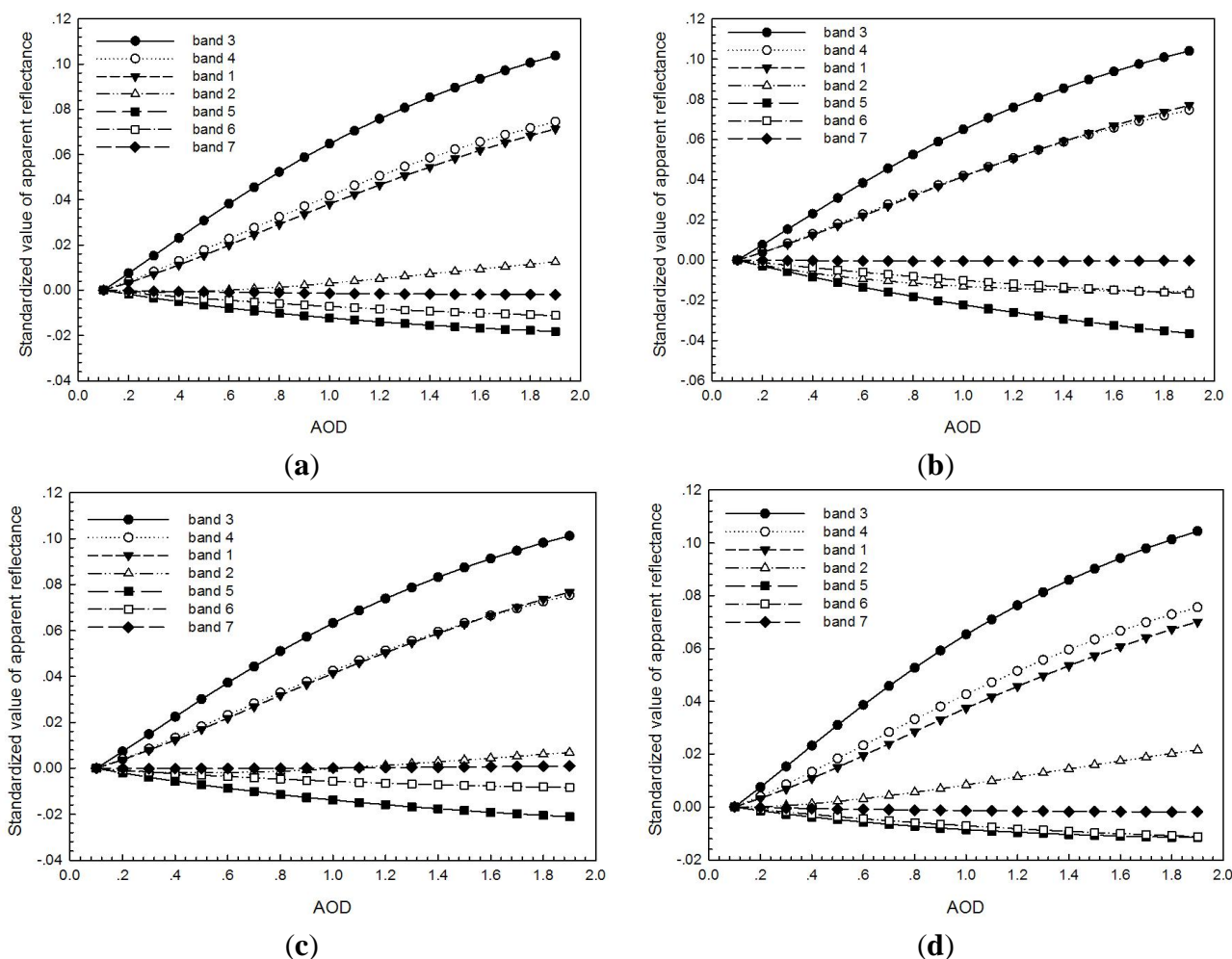
3.3. Variation of Simulated Apparent Reflectance

For the convenience of comparison, the difference between the apparent reflectance of each waveband simulated using the 6S model and apparent reflectance at AOD = 0.1 was used to reveal the variation of apparent reflectance of each waveband with AOD intuitively (Figure 4).

As shown in Figure 4, apparent reflectance simulated from the visible light channels of Band 3 (0.47 μm), Band 4 (0.55 μm), and Band 1 (0.66 μm) of MODIS is rather sensitive to AOD. Apparent reflectance increases with AOD. And the slope for the curve of Band 3 (0.47 μm) relating apparent reflectance to AOD is larger than that of other wavebands. The increase from the initial AOD of 0.1 is the largest in the blue light Band 3 at a magnitude of 0.104 (summer). In addition, a similar trend of increase with AOD is also found in the near infrared Band 2 (0.86 μm) in all other seasons. In contrast, apparent reflectance is related inversely to AOD in the infrared channels of Band 5 (1.24 μm) and Band 6 (1.64 μm) in all four seasons. Apparent reflectance simulated from the infrared Band 7 (2.13μm) is hardly subject to the influence of AOD. In other words, with the increase in AOD, apparent reflectance is almost the same as the surface reflectance. Both are true representation of the inherent optical properties of ground objects.

Figure 4. Relationship between apparent reflectance simulated using the 6S model with AOD by MODIS wavebands. (**a**) spring; (**b**) summer; (**c**) autumn; (**d**) winter.

The influence of AOD on apparent reflectance is suppressed at a longer wavelength because the larger dimension of wavelength than aerosol diameter undermines backscattering. Strong scattering of blue light by aerosols (Figure 3) and the low reflection of blue light by the Earth's surface (Figure 2) make the MODIS blue channel (Band 3) contain the most information on path radiation whereas band 7 is not subject to such an influence. Therefore, it is concluded that apparent reflectance is the most sensitive to AOD in Band 3 (0.47 μm), but least sensitive in Band 7 (2.13 μm). These two bands were thus used to construct three aerosol indices (AI). They are difference aerosol index (DAI), ratio aerosol index (RAI), as well as normalized difference aerosol index (NDAI) using the following equations, respectively:

$$DAI = Band\ 3 - Band\ 7 \tag{2}$$

$$RAI = Band\ 3/Band\ 7 \tag{3}$$

$$NDAI = (Band\ 3 - Band\ 7)/(Band\ 3 + Band\ 7) \tag{4}$$

Listed in Table 3 are the correlation coefficients between the aforementioned indices and AOD in four seasons. These coefficient values demonstrate that under the simulation conditions, each of the indices bears a high linear relationship with AOD. In addition to aerosol, atmospheric absorption gas such as water vapor, ozone, and oxygen all have influence on satellite reflectance in the visible and near-infrared spectrums. By using the default values for the related parameters in the theoretical model, it disturbs the simulative apparent reflectance relatively less, and its calculating results for aerosol indices are more accurate relatively. Therefore, the seasonal variation of correlation coefficients is close. As shown in Table 3, NDAI has the loosest correlationof the three indices. Even so, the minimum correlation coefficient is still as high as 0.9669 in autumn. These results suggest that the proposed aerosol indices can effectively indicate AOD under the simulation conditions. However, the digital images collected by image sensors are generally contaminated in the process of data acquisition, digitization, compression, and transmission. The influenced factors are various and much more complex. Therefore, errors will be inevitably introduced under the actual atmospheric conditions.

Table 3. Correlation coefficient between aerosol indices (AI) and AOD in four seasons.

Season / AI	Spring	Summer	Autumn	Winter
DAI	0.9905	0.9903	0.9902	0.9904
RAI	0.9911	0.9893	0.9875	0.9909
NDAI	0.9707	0.9679	0.9669	0.9704

3.4. Correlation between in situ *Measured AOD and Aerosol Indices*

In order to assess the applicability of the proposed aerosol indices in estimating aerosol-induced atmospheric pollution, the *in situ* measured AOD data at the Lake Taihu station were correlated with aerosol indices calculated from MODIS-derived apparent reflectance by seasons (Table 4). The scatter plots are shown in the Appendix (Figure A1).

Given that the actual atmospheric conditions differ from the standard atmospheric conditions used in the 6S simulation, and that surface reflectance varies with time, errors will be inevitably introduced

to the results if *in situ* measured data were used to construct the model. Judging from the year-long data statistically, the linear correlation between AOD and the three proposed aerosol indices is the closest in summer, but the loosest in winter. A plausible explanation is that AOD in winter over the study site hardly varied, causing a high degree of uncertainty in the retrieved results (Table 2). Since AOD exhibits a relatively large pace of variation both temporally and spatially, and the *in situ* measured results at the Lake Taihu station do not completely match the satellite imagery-derived counterparts. Such spatiotemporal disparity has also contributed to their deviation from the simulated results. Finally, the close proximity of the study site to the lake water means that a huge quantity of water vapor originating from the lake has also exerted an influence on the retrieved AOD for this region. In the literature it has been reported that relative humidity of a study area, to a large extent, is the lead factor influencing AOD [35].

Table 4. Correlation coefficient between aerosol indices and *in situ* measured AOD.

Site	Season	Index	Model	R	R-Squared	P	N
Taihu	Spring	DAI	Y = 4.343 × x + 0.218	0.585	0.343	0.000	
		RAI	Y = 0.160 × x + 0.252	0.378	0.143	0.016	40
		NDAI	Y = 0.763 × x + 0.330	0.380	0.145	0.015	
	Summer	DAI	Y = 10.044 × x − 0.466	0.860	0.740	0.000	
		RAI	Y = 0.411 × x − 0.504	0.656	0.430	0.000	36
		NDAI	Y = 2.669 × x − 0.523	0.623	0.389	0.000	
	Autumn	DAI	Y = 5.440 × x − 0.004	0.685	0.469	0.000	
		RAI	Y = 0.285 × x − 0.149	0.546	0.298	0.001	33
		NDAI	Y = 2.056 × x − 0.289	0.571	0.326	0.001	
	Winter	DAI	Y = 1.716 × x + 0.279	0.333	0.111	0.038	
		RAI	Y = 0.068 × x + 0.319	0.181	0.033	0.270	39
		NDAI	Y = 0.513 × x + 0.273	0.200	0.040	0.223	

Notes: Y: The dependent variable is AOD (550 nm). x: The independent variables are DAI, RAI and NDAI, respectively.

R: correlation coefficient; R-squared: goodness of fit; P: significant coefficient; N: Number of observations.

A comparison of the three indices in a given season demonstrates that difference aerosol index (DAI) has the highest correlation with AOD. This correlation is as high as 0.585 in spring, 0.860 in summer, 0.685 in autumn, and 0.333 in winter. These four correlation coefficients are all significant at the 0.05 significance level. Moreover, the correlation in summer, spring and autumn is still significant at the 0.01 significance level. The spectral index is designed to effectively synthesize the relevant spectral signal, enhance the information of target objects, and decrease the interference of the extra information. Thus far a number of indices, such as NDVI, NDWI, and NDBI, have been used routinely to depict ground objects quantitatively. Similarly, it is assumed that in a clear-sky (non-cloudy) scene, the solar radiation backscattered from aerosols have different spectral signatures with either the Earth's surface or atmospheric molecules. By using multiple bands in the visible, near-IR, and IR wavelength regions, one can perform a retrieval to back out the aerosol signature, and infer the physical properties of the aerosols within the scene. However, dissimilar to ground objects, aerosols are solid or liquid substances suspended in the atmosphere. Their spectral properties are inevitably affected by the characteristics of underlying ground objects. Both RAI and DNAI involve ratioing, which makes them more effective than DAI in suppressing the contribution of weak signals of aerosols to observed

apparent reflectance from the satellite to a large degree. Therefore, DAI is a more suitable indicator of aerosol-related atmospheric pollution than the other two indices.

In addition, to investigate if the proposed method can be applied to other places, the observational data at the AERONET Beijing and Xianghe stations over June 2011–May 2012 were also analyzed. The two stations are situated in Northern China, where the environment is different from Lake Taihu with the colder and drier climate.

The Beijing site (39.98 °N, 116.38 °E) is located on a terrace on the roof of the Institute of Atmospheric Physics building in Beijing. The main land-use types around this site are roads and residential areas. The Xianghe site (39.75 °N, 116.96 °E) is located on the roof of a four-floor building of Xianghe Observatory, Institute of Atmospheric Physics. This site is surrounded by a small town in the east and by agricultural fields in the remaining directions.

The analysis results also show that DAI bears a relatively high correlation with AOD measured with a CE-318 sun photometer in all four seasons (Table 5). The summer and autumn AOD have much correlation with DAI calculated from MODIS-derived apparent reflectance. The scatter plots are also shown in the Appendix (Figures A2 and A3).

Table 5. Correlation coefficient between aerosol indices and *in situ* measured AOD.

Site	Season	Index	Model	R	R-Squared	P	N
Beijing	Spring	DAI	$Y = 6.176 \times x + 0.205$	0.721	0.520	0.000	
		RAI	$Y = 0.721 \times x - 0.488$	0.630	0.397	0.000	32
		NDAI	$Y = 1.973 \times x + 0.215$	0.602	0.363	0.000	
	Summer	DAI	$Y = 13.915 \times x - 0.143$	0.839	0.704	0.000	
		RAI	$Y = 1.022 \times x - 0.752$	0.499	0.249	0.007	28
		NDAI	$Y = 3.581 \times x + 0.121$	0.513	0.263	0.005	
	Autumn	DAI	$Y = 4.951 \times x - 0.091$	0.795	0.632	0.000	
		RAI	$Y = 0.483 \times x - 0.530$	0.695	0.483	0.000	31
		NDAI	$Y = 1.884 \times x - 0.155$	0.653	0.426	0.000	
	Winter	DAI	$Y = 2.952 \times x + 0.001$	0.629	0.396	0.000	
		RAI	$Y = 0.307 \times x - 0.279$	0.601	0.361	0.000	63
		NDAI	$Y = 1.237 \times x - 0.060$	0.583	0.340	0.000	
Xianghe	Spring	DAI	$Y = 7.141 \times x + 0.748$	0.778	0.606	0.000	
		RAI	$Y = 1.543 \times x - 0.804$	0.761	0.580	0.000	36
		NDAI	$Y = 2.801 \times x + 0.766$	0.754	0.569	0.000	
	Summer	DAI	$Y = 11.138 \times x + 0.477$	0.782	0.612	0.000	
		RAI	$Y = 1.184 \times x - 0.700$	0.658	0.433	0.000	30
		NDAI	$Y = 3.257 \times x + 0.514$	0.642	0.413	0.000	
	Autumn	DAI	$Y = 8.392 \times x + 0.131$	0.837	0.701	0.000	
		RAI	$Y = 1.072 \times x - 0.928$	0.794	0.631	0.000	56
		NDAI	$Y = 3.188 \times x + 0.119$	0.769	0.591	0.000	
	Winter	DAI	$Y = 3.742 \times x + 0.275$	0.643	0.413	0.000	
		RAI	$Y = 0.678 \times x - 0.408$	0.643	0.413	0.000	71
		NDAI	$Y = 1.559 \times x + 0.290$	0.621	0.385	0.000	

Notes: Y: The dependent variable is AOD (550 nm). x: The independent variables are DAI, RAI and NDAI, respectively.

R: correlation coefficient; R-squared: goodness of fit; P: significant coefficient; N: Number of observations.

4. Conclusions

The influence of AOD on apparent reflectance is suppressed at a longer wavelength because the larger dimension of wavelength than aerosol diameter undermines backscattering. With the assistance of the 6S radiative transfer model, the response of apparent reflectance in each of MODIS wavebands in relation to AOD was simulated. It was found that strong scattering of blue light by aerosols and the low reflection of blue light by the Earth's surface make the MODIS blue channel (Band 3) contain the most information on path radiation whereas band 7 is not subject to such an influence. This simulation helped to ascertain that apparent reflectance is the most sensitive to AOD in the blue light channel (Band 3), but the least sensitive in the mid-infrared channel (Band 7). Three indices, DAI, RAI, and NDAI, are proposed in this study to determine AOD quickly in a manner similar to NDVI, NDWI, and NDBI that have found wide applications in remote sensing. *In situ* observed AOD data at the AERONET Lake Taihu, Beijing, and Xianghe stations over one year were analyzed in relation to the three proposed aerosol indices. It is concluded that DAI is the most indicative of atmospheric pollution caused by aerosols. DAI bears a relatively high correlation with AOD measured with a CE-318 sun photometer in all four seasons. Such a close correlation demonstrates that the proposed aerosol indices enable effective monitoring of aerosol pollutants from satellite imagery with relative ease.

Acknowledgments

Author Contributions

All authors contributed extensively to the work presented in this paper.

Conflict of Interest

The authors declare no conflict of interest.

References

1. Rosenfeld, D.; Dai, J.; Yu, X.; Yao, Z.Y.; Xu, X.H.; Yang, X.; Du, C.L. Inverse relations between amounts of air pollution and orographic precipitation. *Science* **2007**, *315*, 1396–1398.
2. Wang, K.C.; Dickinson, R.E.; Liang, S.L. Clear sky visibility has decreased over land globally from 1973 to 2007. *Science* **2009**, *323*, 1468–1470.
3. Chan, Y.C.; Simpson, R.W.; Mctainsh, G.H.; Vowles, P.D.; Cohen, D.D.; Bailey, G.M. Source apportionment of visibility degradation problems in Brisbane (Australia) using the multiple linear regression techniques. *Atmos. Environ.* **1999**, *33*, 3237–3250.

4. Carmichael, G.R.; Adhikary, B.; Kulkarni, S.; D'Allura, A.; Tang, Y.H.; Streets, D.; Zhang, Q.; Bond, T.C.; Ramanathan, V.; Jamroensan, A.; *et al.* Asian aerosols: current and year 2030 distributions and implications to human health and regional climate change. *Environ. Sci. Technol.* **2009**, *43*, 5811–5817.

5. Gao, J.; Zha, Y. Meteorological influence on predicting air pollution from MODIS-derived aerosol optical thickness: A case study in Nanjing, China. *Remote Sens.* **2010**, *2*, 2136–2147.

6. Kaufman, Y.J.; Sendra, C. Algorithm for automatic atmospheric corrections to visible and near-IR satellite imagery. *Int. J. Remote Sens.* **1988**, *9*, 1357–1381.

7. Tanré, D.; Deschamps, P.Y.; Devaux, C.; Herman, M. Estimation of Saharan aerosol optical thickness from blurring effects in thematic mapper data. *J. Geophys. Res.* **1988**, *93*, 15955–15964.

8. Holben, B.; Vermote, E.; Kaufman, Y.J.; Tanré, D.; Kalb, V. Aerosols retrieval over land from AVHRR data—Application for atmospheric correction. *IEEE Trans. Geosci. Remote Sens.* **1992**, *30*, 212–222.

9. Herman, M.; Deuzé, J.L.; Devaux, C.; Goloub, P.; Bréon, F.M.; Tanré, D. Remote sensing of aerosols over land surfaces including polarization measurements and application to POLDER measurements. *J. Geophys. Res.* **1997**, *102*, 17039–17049.

10. Deuzé, J.L.; Bréon, F.M.; Devaux, C.; Goloub, P.; Herman, M.; Lafrance, B.; Maignan, F.; Marchand, A.; Nadal, F.; Perry, G.; *et al.* Remote sensing of aerosols over land surfaces from POLDER-ADEOS-1 polarized measurements. *J. Geophys. Res.* **2001**, *106*, 4913–4926.

11. Martonchik, J.V. Determination of aerosol optical depth and land surface directional reflectances using multiangle imagery. *J. Geophys. Res.* **1997**, *102*, 17015–17022.

12. Diner, D.J.; Martonchik, J.V.; Kahn, R.A.; Pinty, B.; Gobron, N.; Nelson, D.L.; Holben, B.N. Using angular and spectral shape similarity constraints to improve MISR aerosol and surface retrievals over land. *Remote Sens. Environ.* **2005**, *94*, 155–171.

13. Hsu, N.C.; Tsay, S.C.; King, M.D.; Herman, J.R. Aerosol properties over bright-reflecting source regions. *IEEE Trans. Geosci. Remote Sens.* **2004**, *42*, 557–569.

14. Rouse, J.W.; Haas, R.H.; Schell, J.A.; Deering, D.W. Monitoring vegetation systems in the Great Plains with ERTS. *NASA Spec. Publ.* **1973**, *1*, 309–317.

15. Mcfeeters, S.K. The use of the normalized difference water index (NDWI) in the delineation of open water features. *Int. J. Remote Sens.* **1996**, *17*, 1425–1432.

16. Zha, Y.; Gao, J.; Ni, S. Use of normalized difference built-up index in automatically mapping urban areas from TM imagery. *Int. J. Remote Sens.* **2003**, *24*, 583–594.

17. Xu, H.Q. Fast information extraction of urban built-up land based on the analysis of spectral signature and normalized difference index. *Geograph. Res.* **2005**, *24*, 311–320. (In Chinese)

18. Griggs, M. Measurement of atmospheric aerosol optical thickness over water using ERTS-1 data. *J. Air Pollut. Control Assoc.* **1975**, *25*, 622–626.

19. Durkee, P.A.; Jensen, D.R.; Hindman, E.E.; VonderHaar, T.H. The relationship between marine aerosol particles and satellite-detected radiance. *J. Geophys. Res.* **1986**, *91*, 4063–4072.

20. Hsu, N.C.; Herman, J.R.; Bhartia, P.K.; Seftor, C.J.; Torres, O.; Thompson, A.M.; Gleason, J.F.; Eck, T.F.; Holben, B.N. Detection of biomass burning smoke from TOMS measurements. *Geophys. Res. Lett.* **1996**, *23*, 745–748.

21. Yu, Z.M.; Zhou, H.M.; Zheng, Y.F. Study on distribution of urban particle pollution by remote sensing and GIS. *J. Nat. Disaster* **2004**, *13*, 58–64. (In Chinese)

22. Zha, Y.; Gao, J.; Jiang, J.J.; Lu, H.; Huang, J.Z. Normalized difference haze index: A new spectral index for monitoring urban air pollution. *Int. J. Remote Sens.* **2012**, *33*, 309–321.

23. Eck, T.F.; Holben, B.N.; Reid, J.S.; Dubovik, O.; Smirnov, A.; O'Neill, N.T.; Slutsker, I.; Kinne, S. Wavelength dependence of the optical depth of biomass burning, urban and desert dust aerosols. *J. Geophys. Res.* **1999**, *104*, 31333–31349.

24. Holben, B.N.; Eck, T.F.; Slutsker, I.; Tanré, D.; Buis, J.P.; Setzer, A.; Vermote, E.; Reagan, J.A.; Kaufman, Y.J.; Nakajima, T.; *et al.* AERONET—A federated instrument network and data archive for aerosol characterization. *Remote Sens. Environ.* **1998**, *66*, 1–16.

25. Aerosol Robotic Network (AERONET). Available online: http://aeronet.gsfc.nasa.gov/ (accessed on 10 January 2013).

26. Dubovik, O.; King, M.D. A flexible inversion algorithm for retrieval of aerosol optical properties from Sun and sky radiance measurements. *J. Geophys. Res.* **2000**, *105*, 20673–20696.

27. National Aeronautics and Space Administration (NASA). Available online: http://ladsweb.nascom.nasa.gov/ (accessed on 10 January 2013).

28. Cao, C.; Xiong, X.; Wu, A.; Wu, X. Assessing the consistency of AVHRR and MODIS L1B reflectance for generating fundamental climate data records. *J. Geophys. Res.* **2008**, *113*, doi:10.1029/2007JD009363.

29. Ångström, A. The parameters of atmospheric turbidity. *Tellus* **1964**, *16*, 64–75.

30. Vermote, E.F.; Tanré, D.; Deuzé, J.L.; Herman, M.; Morcrette, J.J. Second simulation of the satellite signal in the solar spectrum, 6S: An overview. *IEEE Trans. Geosci. Remote Sens.* **1997**, *35*, 675–686.

31. Hu, F.C.; Wang, Z.H.; Zhang, B.; Li, J.S. Study on method for determining atmospheric aerosol type using remote sensing experimental Data. *Chin. J. Lasers* **2009**, *36*, 312–317. (In Chinese)

32. Vermote, E.F.; Tanré, D.; Deuzé, J.L.; Herman, M.; Morcrette, J.J.; Kotchenova, S.Y. *Second Simulation of the Satellite Signal in the Solar Spectrum (6S)*; 6S User Guide Version 3, November 2006. Available online: http://6s.ltdri.org (accessed on 18 October 2013).

33. Zhang, J.H.; Si, Z.J.; Mao, J.T.; Wang, M.H. Remote sensing aerosol optical depth over China with GMS-5 satellite. *Chin. J. Atmos. Sci.* **2003**, *27*, 23–35. (In Chinese)

34. Rao, J.W.; Ma, R.H.; Duan, H.T.; Jiang, G.J.; Shang, L.L.; Zhou, L. Aerosol optical thickness of the atmospheric aerosol over Taihu Lake and its features: Results of *in situ* measurements. *Environ. Sci.* **2012**, *33*, 2158–2164. (In Chinese)

35. Zhang, L.; Liao, H.; Li, J.P. Impacts of Asian summer monsoon on seasonal and interannual variations of aerosols over eastern China. *J. Geophys. Res.* **2010**, *115*, doi:10.1029/2009JD012299.

Appendix

Table A1. The statistics for all of the level 2.0 AOD (550 nm) as observed at the Lake Taihu station.

Season	Seasonal Mean
Spring	0.61 ± 0.27
Summer	0.72 ± 0.52
Autumn	0.55 ± 0.33
Winter	0.51 ± 0.22

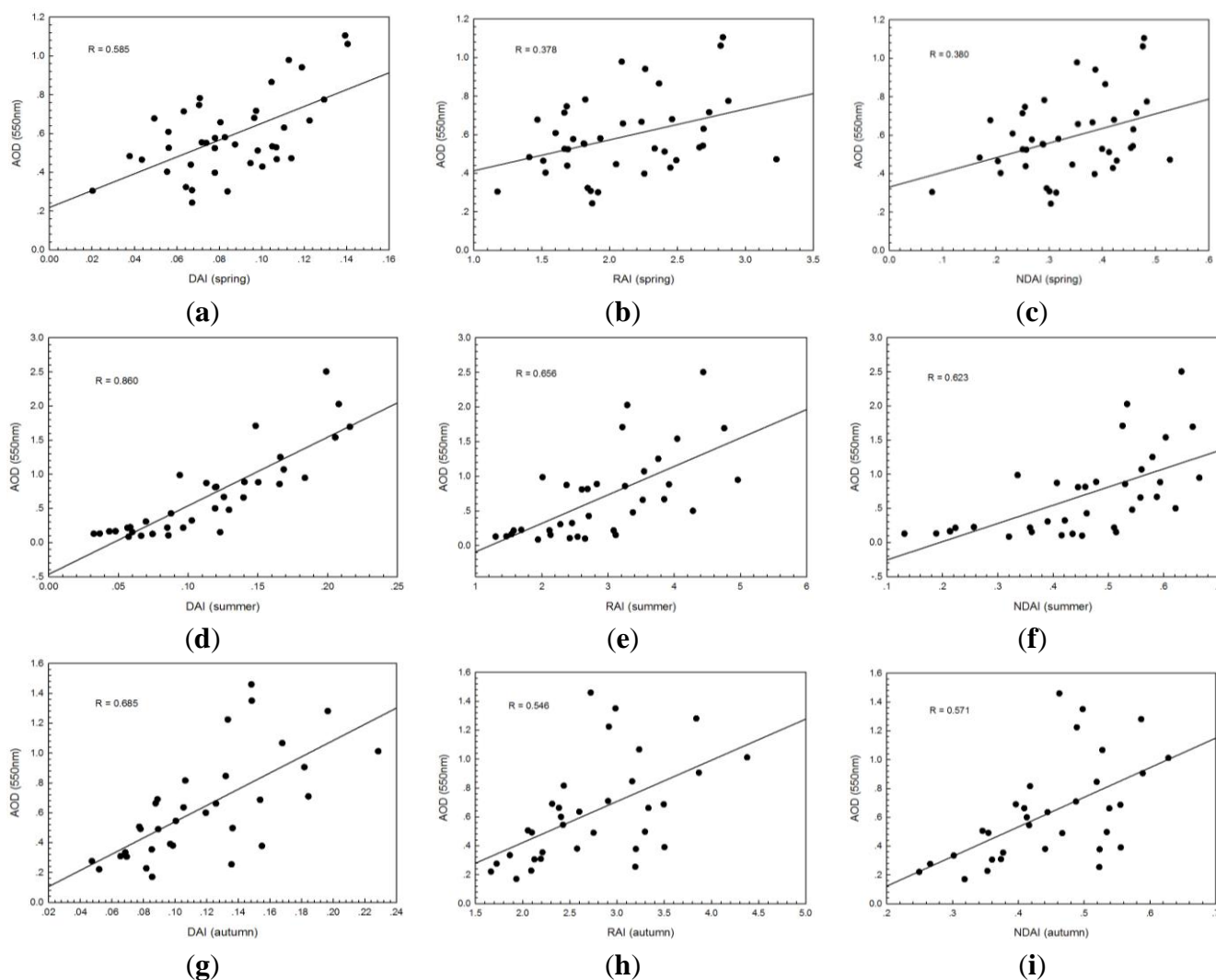**Figure A1.** Regression results of the three proposed aerosol indices (DAI, RAI, NDAI) against AOD (550 nm) as observed at the Lake Taihu station. (**a**–**c**) spring; (**d**–**f**) summer; (**g**–**i**) autumn; (**j**–**l**) winter.

(**a**)   (**b**)   (**c**)

(**d**)   (**e**)   (**f**)

(**g**)   (**h**)   (**i**)

Figure A1. *Cont.*

(**j**)   (**k**)   (**l**)

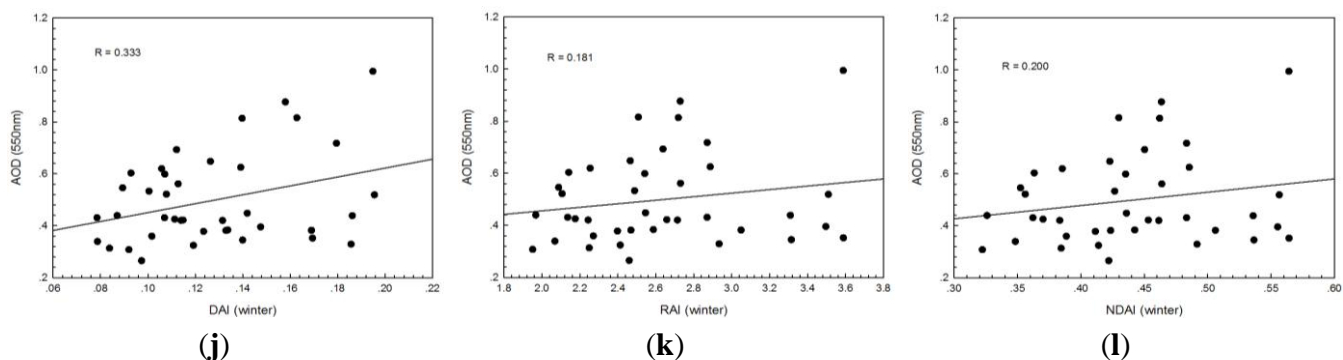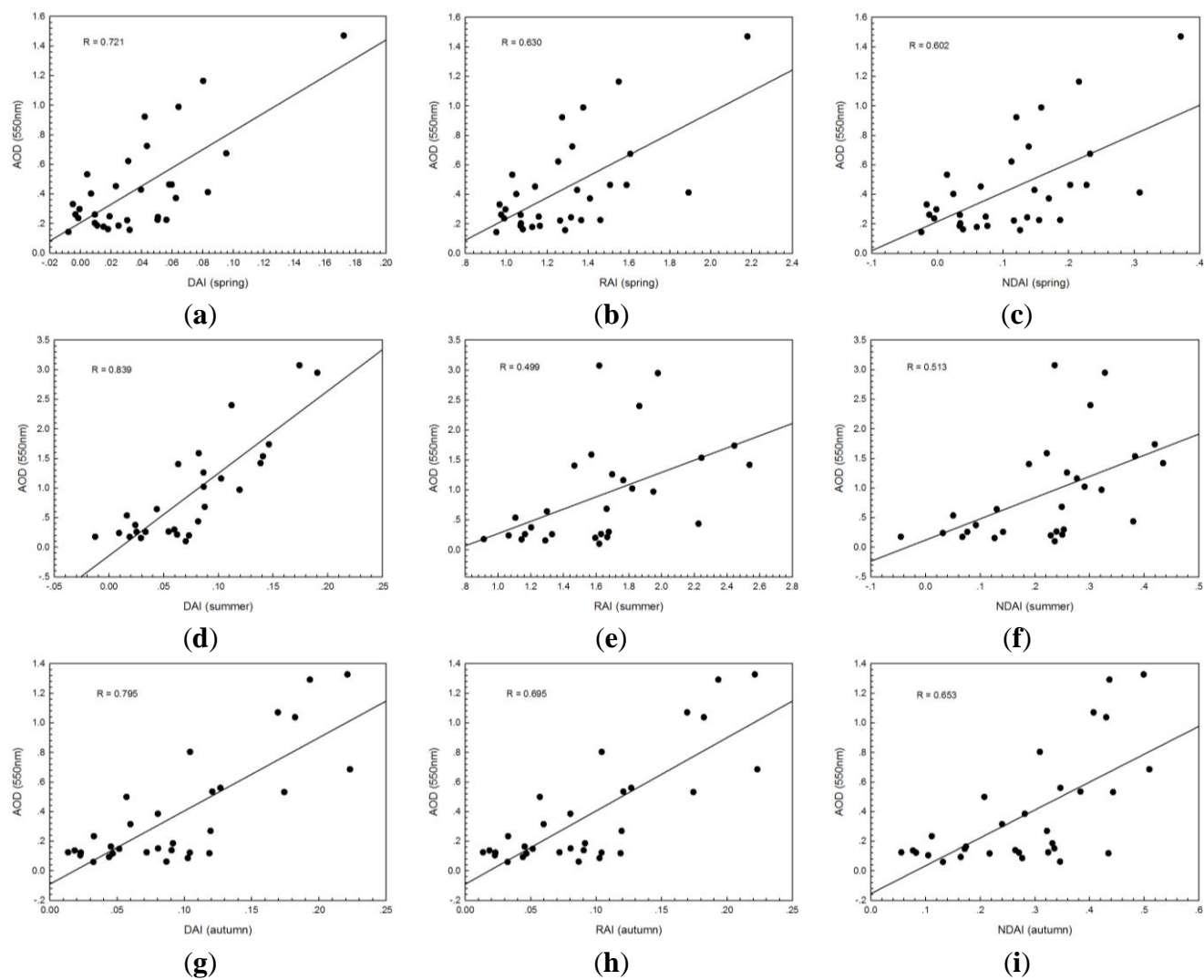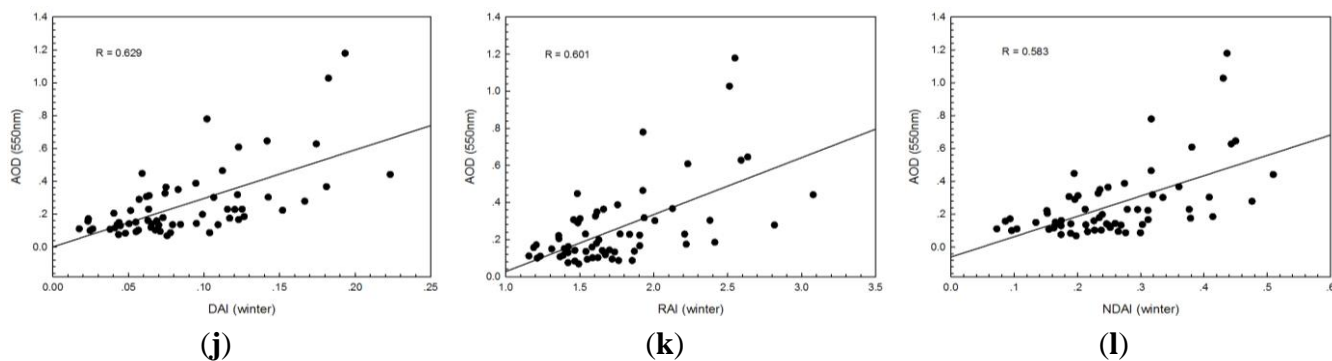**Figure A2.** Regression results of the three proposed aerosol indices (DAI, RAI, NDAI) against AOD (550 nm) as observed at the Beijing station. (**a**–**c**) spring; (**d**–**f**) summer; (**g**–**i**) autumn; (**j**–**l**) winter.

(**a**)   (**b**)   (**c**)

(**d**)   (**e**)   (**f**)

(**g**)   (**h**)   (**i**)

Figure A2. *Cont.*

(**j**)   (**k**)   (**l**)

Figure A3. Regression results of the three proposed aerosol indices (DAI, RAI, NDAI) against AOD (550 nm) as observed at the Xianghe station. (**a**–**c**) spring; (**d**–**f**) summer; (**g**–**i**) autumn; (**j**–**l**) winter.
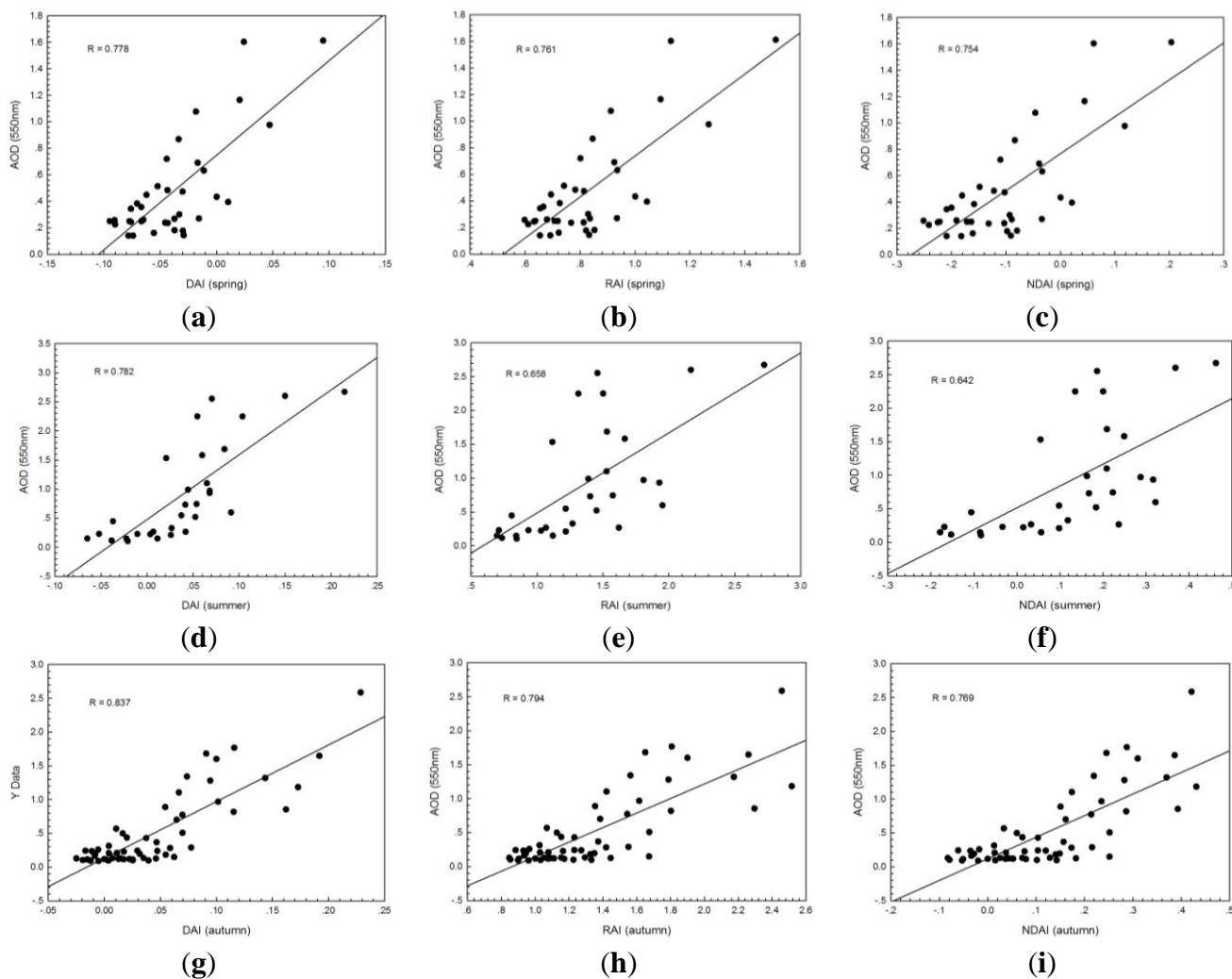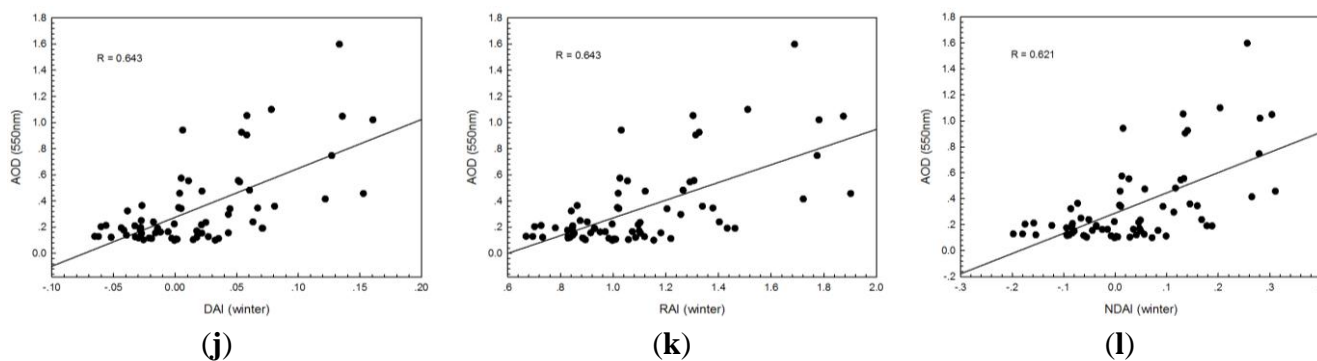

(**a**)   (**b**)   (**c**)

(**d**)   (**e**)   (**f**)

(**g**)   (**h**)   (**i**)

Figure A3. *Cont.*

(**j**)　　　　　　　　　(**k**)　　　　　　　　　(**l**)